

Strong Spin-Orbit Torque Induced by the Intrinsic Spin Hall Effect in $\text{Cr}_{1-x}\text{Pt}_x$

Qianbiao Liu¹, Jingwei Li², Lujun Zhu³, Xin Lin¹, Xinyue Xie³, and Lijun Zhu^{1,4,*}

¹State Key Laboratory of Superlattices and Microstructures, Institute of Semiconductors, Chinese Academy of Sciences, Beijing 100083, China

²Multi-scale Porous Materials Center, Institute of Advanced Interdisciplinary Studies & School of Chemistry and Chemical Engineering, Chongqing University, Chongqing 400044, China

³College of Physics and Information Technology, Shaanxi Normal University, Xi'an 710062, China

⁴College of Materials Science and Opto-Electronic Technology, University of Chinese Academy of Sciences, Beijing 100049, China

(Received 8 July 2022; revised 30 August 2022; accepted 11 October 2022; published 23 November 2022)

We report on a spin-orbit-torque study of the spin-current generation in $\text{Cr}_{1-x}\text{Pt}_x$ alloy, using the light 3d ferromagnetic Co as the spin-current detector. We find that the dampinglike spin-orbit torque of $\text{Cr}_{1-x}\text{Pt}_x/\text{Co}$ bilayers can be enhanced by tuning the Cr concentration in the $\text{Cr}_{1-x}\text{Pt}_x$ layer, with a maximal value of 0.31 at the optimal composition of $\text{Cr}_{0.2}\text{Pt}_{0.8}$. The mechanism and the efficiency of spin-current generation in the $\text{Cr}_{1-x}\text{Pt}_x$ alloy can be fully understood by the characteristic trade-off between the intrinsic spin Hall conductivity of Pt and the spin carrier lifetime in the dirty limit. This suggests that Cr is simply as effective as other metals, oxides, and nitrides (e.g., Hf, Au, Pd, Cu, Ti, MgO, and Si_3N_4) in enhancing the dampinglike spin-orbit torque generated by the spin Hall effect of a Pt host via strengthening the spin carrier scattering and that alloying Pt with Cr does not employ observable spin-current generation via additional spin Hall effect, orbital Hall effect, or interfacial spin-orbit coupling effects. This work also establishes the low-resistivity $\text{Cr}_{0.2}\text{Pt}_{0.8}$ as an energy-efficient spin-orbit-torque provider for magnetic memory and computing technologies.

DOI: 10.1103/PhysRevApplied.18.054079

I. INTRODUCTION

Strong spin-orbit torques (SOTs) have the potential to efficiently manipulate magnetization in nonvolatile memory and computing technologies [1–9]. In the simple case of heavy metal/light 3d ferromagnet metal (HM/FM) in which the spin Hall effect (SHE) of the HM is the dominant source of the spin current and the spin current diffused into the FM relaxes mainly via the exchange interaction with the magnetization, the dampinglike SOT efficiency (ξ_{DL}^j) is approximately the product of the spin Hall ratio (θ_{SH}) of the HM and the spin transparency (T_{int}) of the HM/FM interface, i.e., $\xi_{\text{DL}}^j \approx T_{\text{int}}\theta_{\text{SH}}$. Consequently, ξ_{DL}^j can be enhanced if θ_{SH} of the HM [10–14] or T_{int} of the HM/FM interface [15–19] can be increased.

Platinum (Pt) is an excellent platform for developing strong spin Hall metals because of the giant intrinsic spin Hall conductivity (σ_{SH}) of approximately equal to $1.6 \times 10^6 (\hbar/2e) \Omega^{-1}\text{m}^{-1}$ in the clean limit [16,20], high electrical conductivity (σ_{xx}), high spin-mixing conductance ($G_{\text{eff}}^{\uparrow\downarrow}$) of $1.3 \times 10^{15} \Omega^{-1}\text{m}^{-2}$ in contact with FM [18,19] and ferrimagnetic metals [21]. Theories

[20] and experiments [22,23] have well established that $\theta_{\text{SH}} = (2e/\hbar)\sigma_{\text{SH}}/\sigma_{xx}$ of a Pt host can be significantly enhanced by optimizing the trade-off between the intrinsic σ_{SH} and the spin carrier lifetime (which is proportional to σ_{xx}). In agreement with this mechanism, the scaling of σ_{SH} with σ_{xx} coincides for various Pt-based alloys and multilayers [19,24].

However, alloying Pt with Cr has been recently reported to be considerably more [25] or substantially less [26] effective in enhancing ξ_{DL}^j than alloys and multilayers of Pt and other metals (e.g., Hf [10], Au [11], Pd [12], Cu [9,14], and Ti [21]), oxides (MgO [13]), or nitrides (Si_3N_4 [27]). It is also surprising that the claimed highest value of ξ_{DL}^j is one order of magnitude greater for $\text{Cr}_{1-x}\text{Pt}_x/\text{Co}$ ($\xi_{\text{DL}}^j = 0.92 \pm 0.07$) in Ref. [25] than for $\text{Cr}_{1-x}\text{Pt}_x/\text{Pt}(0.4)/\text{Co}$ ($\xi_{\text{DL}}^j \approx 0.1$) in Ref. [26] despite the same spin-current generating material $\text{Cr}_{1-x}\text{Pt}_x$ and the same loop shift-measurement technique. It is particularly motivating to establish in-depth understanding of the spin-current physics of the $\text{Cr}_{1-x}\text{Pt}_x$ alloy and to clarify the discrepancies in the literature since Cr is a light metal that has been reported to have rich manifestations such as negative [28,29], positive θ_{SH} [30], orbital Hall effect [31,32], and antiferromagnetism [29] in its film form.

*ljzhu@semi.ac.cn

In this work, we examine the spin-current generation in $\text{Cr}_{1-x}\text{Pt}_x$ alloy using the light 3d ferromagnetic Co as the spin-current detector. We find that ξ_{DL}^j for $\text{Cr}_{1-x}\text{Pt}_x/\text{Co}$ bilayers can be enhanced to 0.31 by tuning the composition of the $\text{Cr}_{1-x}\text{Pt}_x$ layer. The mechanism and the efficiency of spin-current generation in the $\text{Cr}_{1-x}\text{Pt}_x$ alloy can be fully understood by the characteristic trade-off between the intrinsic spin Hall conductivity of Pt and the carrier lifetime in the dirty limit. This reveals that Cr is simply as effective as other metals and oxides (e.g., Au, Pd, Cu, Ti, MgO, and Si_3N_4) [9–14,21–23,27] in enhancing ξ_{DL}^j via strengthening the spin carrier scattering in the Pt host.

II. RESULTS AND DISCUSSIONS

A. Samples and characterizations

The samples for this work include in-plane magnetic anisotropy (IMA) bilayers of $\text{Cr}_{1-x}\text{Pt}_x(5)/\text{Co}(1.3)$ and perpendicular magnetic anisotropy (PMA) bilayers of $\text{Cr}_{1-x}\text{Pt}_x(5)/\text{Co}(0.48)$ (numbers are thicknesses in nm) with different Pt concentration (x), as well as IMA $\text{Cr}_{1-x}\text{Pt}_x(d)/\text{Co}(1.3)$ with different $\text{Cr}_{1-x}\text{Pt}_x$ thickness (d). Each sample is sputter deposited on a Si/SiO₂ substrate at room temperature with a 1-nm Ta adhesion layer and

protected by a MgO(1.6)/Ta(1.5) bilayer. The 1-nm Ta adhesion layer is highly resistive and contributes negligible spin current into the Co. The top Ta capping layer is fully oxidized upon exposure to the atmosphere. Scanning transmission electron microscopy image and electron-dispersive x-ray spectrum mapping results in Fig. 1(a) reveal good elemental uniformity of Cr and Pt within the $\text{Cr}_{1-x}\text{Pt}_x$ layer, polycrystalline structure with large lateral grain size of 15 nm, and reasonably sharp interface with the Co layer. High-resolution STEM images of the interface regions [Fig. 1(b)] indicate face-centered cubic (fcc) structure for both Co and $\text{Cr}_{1-x}\text{Pt}_x$ layers and epitaxial growth of Co layer on top of the $\text{Cr}_{1-x}\text{Pt}_x$ along (111) orientation. This is consistent with previous reports that $\text{Cr}_{1-x}\text{Pt}_x$ alloy prepared at room-temperature crystallizes into the chemically disordered fcc structure in the composition range of $x \geq 0.4$ [33]. Atomic force microscopy measurements [Fig. 1(c)] indicate that our $\text{Cr}_{1-x}\text{Pt}_x$ layers have fairly smooth surfaces in a large scale, for instance, with a small square-root surface roughness of 0.3 nm for the $\text{Cr}_{1-x}\text{Pt}_x$ with $x = 0.2$. X-ray diffraction θ -2 θ patterns show only the fcc (111) peaks for all the $\text{Cr}_{1-x}\text{Pt}_x$ layers studied in this work [Fig. 1(d)], reaffirming that the $\text{Cr}_{1-x}\text{Pt}_x$ forms a chemically disordered fcc alloy with

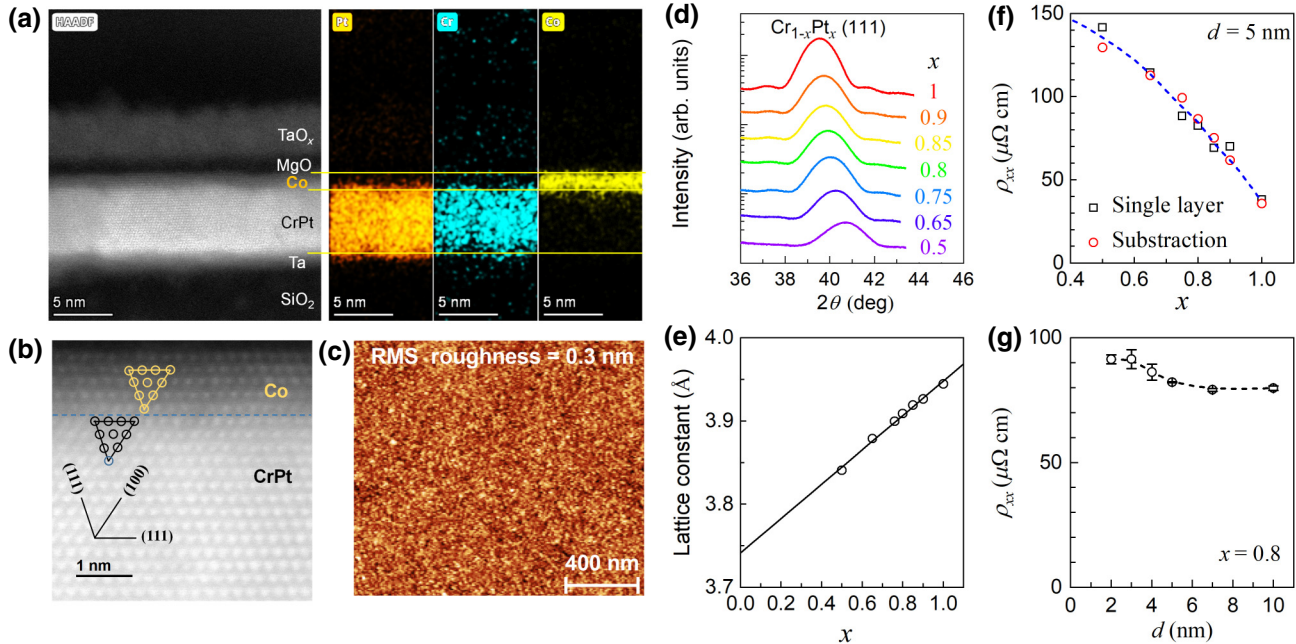


FIG. 1. (a) Cross-section scanning transmission electron microscopy image and electron dispersive x-ray spectrum mapping of Pt, Cr, and Co for a $\text{Cr}_{0.2}\text{Pt}_{0.8}(5)/\text{Co}(1.3)$ sample. (b) High-resolution scanning transmission electron microscopy image of the interface of the $\text{Cr}_{0.2}\text{Pt}_{0.8}(5)/\text{Co}(1.3)$ bilayer, suggesting the epitaxial growth of Co on $\text{Cr}_{1-x}\text{Pt}_x$. (c) Atomic force microscopy image ($2 \times 2 \mu\text{m}^2$ in area) of the $\text{Cr}_{0.2}\text{Pt}_{0.8}(5)/\text{Co}(1.3)$ sample, indicating a small square-root roughness of 0.3 nm. (d) X-ray diffraction patterns of the $\text{Cr}_{1-x}\text{Pt}_x(5)/\text{Co}(1.3)$ with different $\text{Cr}_{1-x}\text{Pt}_x$ compositions. (e) Lattice constant of $\text{Cr}_{1-x}\text{Pt}_x$ plotted as a function of x . (f) x dependence of ρ_{xx} for the $\text{Cr}_{1-x}\text{Pt}_x$ as determined by measuring the resistivity of control $\text{Cr}_{1-x}\text{Pt}_x$ single layers (black squares) and by subtracting the conductance of control stacks $\text{Ta}(1)/\text{Co}(0.48)$, $(1.3)/\text{MgO}(1.6)/\text{Ta}(1.6)$ from the whole stack $\text{Ta}(1)/\text{Cr}_{1-x}\text{Pt}_x(d)/\text{Co}(0.48)$, $(1.3)/\text{MgO}(1.6)/\text{Ta}(1.6)$ (red circles). (g) The averaged resistivity for the $\text{Cr}_{1-x}\text{Pt}_x$ with different thicknesses. Dashed lines in (c),(g),(h) are to guide the eyes.

preferred (111) orientation. From the $\text{Cr}_{1-x}\text{Pt}_x$ (111) peak, which shifts increasingly more to a higher 2θ angle with increasing Cr concentration, we determine that the average lattice constant of the $\text{Cr}_{1-x}\text{Pt}_x$ is a linear function of the Pt concentration [Fig. 1(e)], in good agreement with Vegard's law.

Superconducting quantum interference device measurements reveal that the saturation magnetization (M_s) is approximately equal to 1370 emu/cm³ for the 1.3 nm Co, approximately equal to 1210 emu/cm³ for the 0.48 nm Co. The dependence on the Co thickness of magnetic moment per area suggests negligible dead layer for these Co layers [Fig. 2(a)]. The $\text{Cr}_{1-x}\text{Pt}_x$ layers are paramagnetic ($M_s \approx 0$ emu/cm³) and show no measurable magnetization or anomalous Hall effect [Figs. 2(b)–2(d)], which is consistent with the literature reports [33,34]. The samples are then patterned by photolithography and ion milling into $5 \times 60 \mu\text{m}^2$ Hall bars followed by deposition of 5-nm Ti and 150-nm Pt as contacts for electrical measurements. The resistivity (ρ_{xx}) for $\text{Cr}_{1-x}\text{Pt}_x$ is determined by measuring the resistivity of control $\text{Cr}_{1-x}\text{Pt}_x$ single layers and by subtracting the conductance of Ta(1)/Co(0.48)(1.3)/MgO(1.6)/Ta(1.6) from that of the whole stack Ta(1)/ $\text{Cr}_{1-x}\text{Pt}_x(d)$ /Co(0.48)(1.3)/MgO(1.6)/Ta(1.6), respectively. As shown in Fig. 1(f), the values of ρ_{xx} determined from the two methods consistently vary from $37 \mu\Omega \text{ cm}$ for $x = 1$ to $135 \mu\Omega \text{ cm}$ for $x = 0.5$. Figure 1(g) shows the dependence on the thickness of the values of ρ_{xx} for the $\text{Cr}_{0.2}\text{Pt}_{0.8}$ as determined by averaging the values estimated from the two methods.

B. Composition dependence of spin-orbit torques

The dampinglike SOT efficiencies of $\text{Cr}_{1-x}\text{Pt}_x(5)/\text{Co}(1.3)$ bilayers ($x \geq 0.5$) are first determined by angle-dependent “in-plane” harmonic Hall voltage response (HHVR) measurements [11,35]. While applying a sinusoidal electric field (E) of 33.3 kV/m onto the bar orientated along the x axis, the in-phase first and out-of-phase second HHVRs, $V_{1\omega}$ and $V_{2\omega}$, are collected as a function of the angle (φ) of the in-plane magnetic field (H_{xy}) with respect to the current under different magnetic field magnitudes (1250–3250 Oe). Within the macrospin approximation,

$$V_{2\omega} = V_{\text{DL+ANE}} \sin \varphi + V_{\text{FL+Oe}} \sin \varphi \cos 2\varphi, \quad (1)$$

where $V_{\text{DL+ANE}} = -V_{\text{AHE}} H_{\text{DL}} / 2(H_{xy} + |H_k|) + V_{\text{ANE}}$, $V_{\text{FL+Oe}} = -V_{\text{PHE}} (H_{\text{FL}} + H_{\text{Oe}}) / 2H_{xy}$, V_{AHE} is the anomalous Hall voltage, V_{PHE} the planar Hall voltage, and V_{ANE} the anomalous Nernst voltage induced by the vertical thermal gradient, H_k the perpendicular anisotropy field. The values of V_{AHE} and H_k are determined from the dependence of $V_{1\omega}$ on the swept out-of-plane field (H_z) under zero H_{xy} [Fig. 3(a)]. The $V_{\text{DL+ANE}}$ of the $\text{Cr}_{1-x}\text{Pt}_x(d)/\text{Co}(1.3)$ for each magnitude of H_{xy} is extracted from the fit of the

φ dependence of $V_{2\omega}$ to Eq. (1) [see Fig. 3(b) for two representative examples for the $\text{Cr}_{0.2}\text{Pt}_{0.8}(5)/\text{Co}(1.3)$]. The slope and the intercept of the linear fit of $V_{\text{DL+ANE}}$ vs $-V_{\text{AHE}} / 2(H_{xy} + |H_k|)$ give the values of H_{DL} and V_{ANE} , respectively [Fig. 3(c)]. Figure 4(a) shows ξ_{DL}^j as calculated following the relation:

$$\xi_{\text{DL}}^j = (2e/\hbar)\mu_0 M_s t_{\text{Co}} H_{\text{DL}} \rho_{xx} / E, \quad (2)$$

with e , μ_0 , t_{Co} , and \hbar being the elementary charge, the permeability of vacuum, the Co thickness, the reduced Planck's constant, respectively. ξ_{DL}^j for the IMA

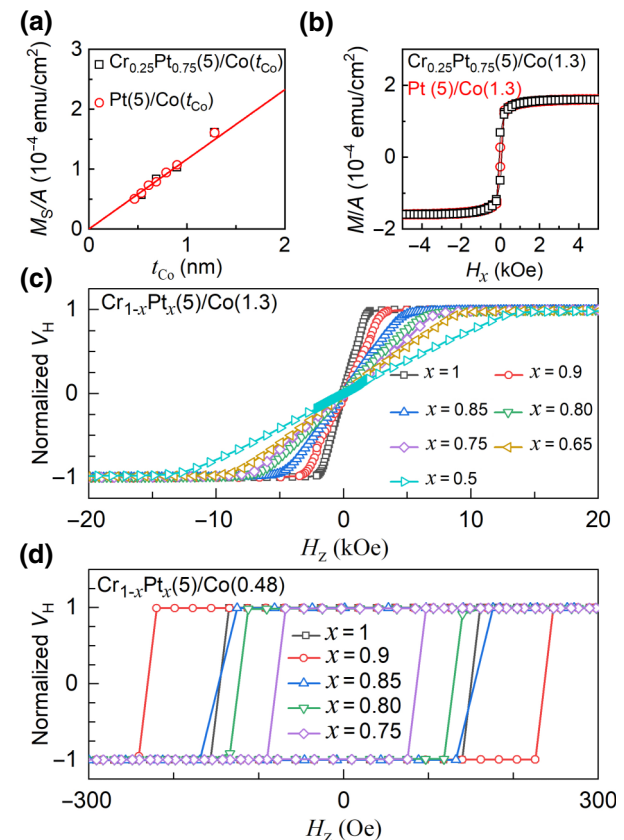


FIG. 2. Absence of magnetic and anomalous Hall voltage contributions from the $\text{Cr}_{1-x}\text{Pt}_x$ layer. (a) In-plane magnetic moment per area vs in-plane magnetic field for the Pt(5 nm)/Co(1.3 nm) and for the $\text{Cr}_{0.25}\text{Pt}_{0.75}(5 \text{ nm})/\text{Co}(1.3 \text{ nm})$, suggesting no difference in saturation magnetization for samples with different Pt concentration and thus no magnetic contribution in the $\text{Cr}_{0.25}\text{Pt}_{0.75}$ layer. (b) The Co thickness dependence of the saturation magnetic moment per area for the $\text{Cr}_{1-x}\text{Pt}_x / \text{Co}$ t_{Co} bilayers, extrapolating zero magnetization at zero Co thickness. (c) In-plane nonhysteretic Hall voltage loops for the $\text{Cr}_{1-x}\text{Pt}_x(5 \text{ nm})/\text{Co}(1.3 \text{ nm})$ samples. (d) Square Hall voltage loops for the $\text{Cr}_{1-x}\text{Pt}_x(5 \text{ nm})/\text{Co}(0.48 \text{ nm})$ samples. The loop shapes in (c),(d) suggest no anomalous Hall voltage contributed by the $\text{Cr}_{1-x}\text{Pt}_x$ layers in the in-plane and out-of-plane directions. These results are well consistent with expectation that the $\text{Cr}_{1-x}\text{Pt}_x$ layers are paramagnetic.

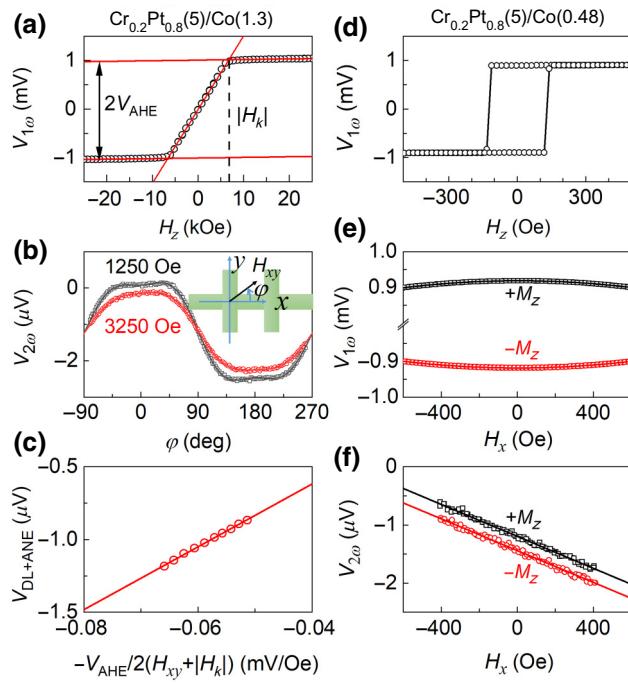


FIG. 3. (a) $V_{1\omega}$ vs H_z . (b) $V_{2\omega}$ vs φ , and (c) $V_{\text{DL}+\text{ANE}}$ vs $-V_{\text{AHE}} H_{\text{DL}} / 2(H_{xy} + |H_k|)$ for the $\text{Cr}_{0.2}\text{Pt}_{0.8}(5)/\text{Co}(1.3)$. (d) $V_{1\omega}$ vs H_z , (e) $V_{1\omega}$ vs H_x , and (f) $V_{2\omega}$ vs H_x for the $\text{Cr}_{0.2}\text{Pt}_{0.8}(5)/\text{Co}(0.48)$. Solid lines in (a),(c),(f) represent linear fits; the solid curves represent fits of the data to Eq. (1) in (b) and to a parabolic function in (e). The inset in (b) shows the measurement coordinate.

$\text{Cr}_{1-x}\text{Pt}_x(5)/\text{Co}(1.3)$ firstly increases from 0.18 at $x = 0$ to the peak value of 0.31 at $x = 0.80$, and then gradually drops to 0.20 at $x = 0.5$. We find a strong anisotropy in the film plane in the $\text{Cr}_{1-x}\text{Pt}_x(5)/\text{Co}(1.3)$ with $x = 0$ and 0.2, preventing analysis of ξ_{DL}^j at those compositions (see Fig. 6 in the Appendix).

We find a similar composition dependence of ξ_{DL}^j for the PMA $\text{Cr}_{1-x}\text{Pt}_x(5)/\text{Co}(0.48)$ bilayers from out-of-plane HHVR measurements [36]. As indicated by the fairly square Hall voltage hysteresis in Fig. 3(d), the $\text{Cr}_{1-x}\text{Pt}_x(5)/\text{Co}(0.48)$ with $x \geq 0.75$ show good PMA, which allows us to perform high-quality out-of-plane HHVR analyses. As we show in Figs. 3(e) and 3(f), $V_{1\omega}$ and $V_{2\omega}$ for the $\text{Cr}_{1-x}\text{Pt}_x(5)/\text{Co}(0.48)$ with $x \geq 0.75$ are well-defined parabolic and linear functions of the in-plane magnetic field H_x , respectively, from which the dampinglike SOT field is determined as $H_{\text{DL}} = -2(\partial V_{2\omega} / \partial H_x) / (\partial^2 V_{1\omega} / \partial H_x^2)$. Note that there is only negligible anomalous Nernst effect [37,38] in our $\text{Cr}_{1-x}\text{Pt}_x(5)/\text{Co}(0.48)$ bilayers (Fig. 7 in the Appendix). We ignore the so-called “planar Hall correction,” which is generally found to cause errors when not negligible [12,39,40] (also see Fig. 8 in the Appendix). As we show in Fig. 4(a), ξ_{DL}^j for the $\text{Cr}_{1-x}\text{Pt}_x(5)/\text{Co}(0.48)$

also peaks at $x \approx 0.80$. Interestingly, the values of ξ_{DL}^j for the $\text{Cr}_{1-x}\text{Pt}_x(5)/\text{Co}(0.48)$ are slightly smaller than that for the $\text{Cr}_{1-x}\text{Pt}_x(5)/\text{Co}(1.3)$. This is likely because the Co thickness of 0.48 nm is smaller than the spin dephasing length of the Co such that a portion of spin current approaches and gets reflected at the top Co/MgO interface. It is expected that the polarization of such reflected spin current is rotated relative to the incident spin current [41,42], which leads to a decrease of the effective SOT exerted on the Co layer. The difference in the torque efficiencies for the PMA $\text{Cr}_{1-x}\text{Pt}_x(5)/\text{Co}(0.48)$ and the IMA $\text{Cr}_{1-x}\text{Pt}_x(5)/\text{Co}(1.3)$ cannot be attributed to spin memory loss because the interfacial magnetic anisotropy energy density (K_s^{ISOC}) is smaller at the $\text{Cr}_{0.2}\text{Pt}_{0.8}(5)/\text{Co}(0.48)$ interface than the $\text{Cr}_{0.2}\text{Pt}_{0.8}(5)/\text{Co}(1.3)$ interface (Fig. 9 in the Appendix). The PMA of the $\text{Cr}_{1-x}\text{Pt}_x(5)/\text{Co}(0.48)$ becomes weak for $x < 0.75$ (Fig. 10 in the Appendix), preventing out-of-plane HHVR analysis.

C. Mechanism of spin-orbit torque

We now show that the spin-current generation in the $\text{Cr}_{1-x}\text{Pt}_x$ is dominated by the intrinsic SHE. As plotted in Fig. 4(b), ξ_{DL}^j and the apparent spin Hall conductivity $T_{\text{int}}\sigma_{\text{SH}} = (\hbar/2e)\xi_{\text{DL}}^j/\rho_{xx}$ of the $\text{Cr}_{0.2}\text{Pt}_{0.8}(d)/\text{Co}(1.3)$ are large constants at large d values and reduce gradually towards zero as d decreases, which is consistent with the SHE being the dominant mechanism of the spin-current generation in the $\text{Cr}_{1-x}\text{Pt}_x$. A more unambiguous piece of evidence for the intrinsic SHE is the characteristic decrease of $T_{\text{int}}\sigma_{\text{SH}}$ of $\text{Cr}_{1-x}\text{Pt}_x(5)/\text{Co}(1.3)$ with σ_{xx} in the dirty limit. Here, T_{int} is set by spin backflow [16,19,43,44] and spin memory loss [17], i.e., $T_{\text{int}} \approx T_{\text{int}}^{\text{SML}} T_{\text{int}}^{\text{SBF}}$ [23,24]. Drift-diffusion model [16,43,44] predicts

$$T_{\text{int}}^{\text{SBF}} = (1 - \text{sech}(d/\lambda_s))(1 + \tanh(d/\lambda_s)/2\lambda_s\rho_{xx}G_{\text{eff}}^{\uparrow\downarrow}), \quad (3)$$

where $1/\lambda_s\rho_{xx} \approx 1.3 \times 10^{15} \Omega^{-1}\text{m}^{-2}$ for Pt [45,46]. Our previous study shows that $T_{\text{int}}^{\text{SML}} \approx 1 - 0.23 K_s^{\text{ISOC}}$ for IMA Pt/Co, with K_s^{ISOC} in erg/cm^2 . The values of K_s^{ISOC} for the interfaces of $\text{Cr}_{1-x}\text{Pt}_x(5)/\text{Co}(1.3)$ are estimated by subtracting the interfacial PMA energy density of approximately equal to 0.6 erg/cm^2 [17] from the total interfacial PMA energy density (K_s) of the two interfaces of the $\text{Cr}_{1-x}\text{Pt}_x(5)/\text{Co}(1.3)/\text{MgO}$ (Fig. 11 in the Appendix). K_s is estimated following the relation $H_k \approx -4\pi M_s + 2K_s M_s t_{\text{Co}}$.

In Fig. 4(c), we compare the values of $T_{\text{int}}\sigma_{\text{SH}}$ and σ_{SH} of the $\text{Cr}_{1-x}\text{Pt}_x(5)/\text{Co}(1.3)$ with those of $\text{Pt}_x(\text{MgO})_x/\text{Co}$ [13], Pt-Hf multilayers/Co [23] and Pt-Ti multilayers/Co [24] as a function of σ_{xx} . Clearly, both $T_{\text{int}}\sigma_{\text{SH}}$ and σ_{SH} for the $\text{Cr}_{1-x}\text{Pt}_x$ follow the characteristic decrease of the *intrinsic* spin Hall conductivity with σ_{xx} in the dirty limit,

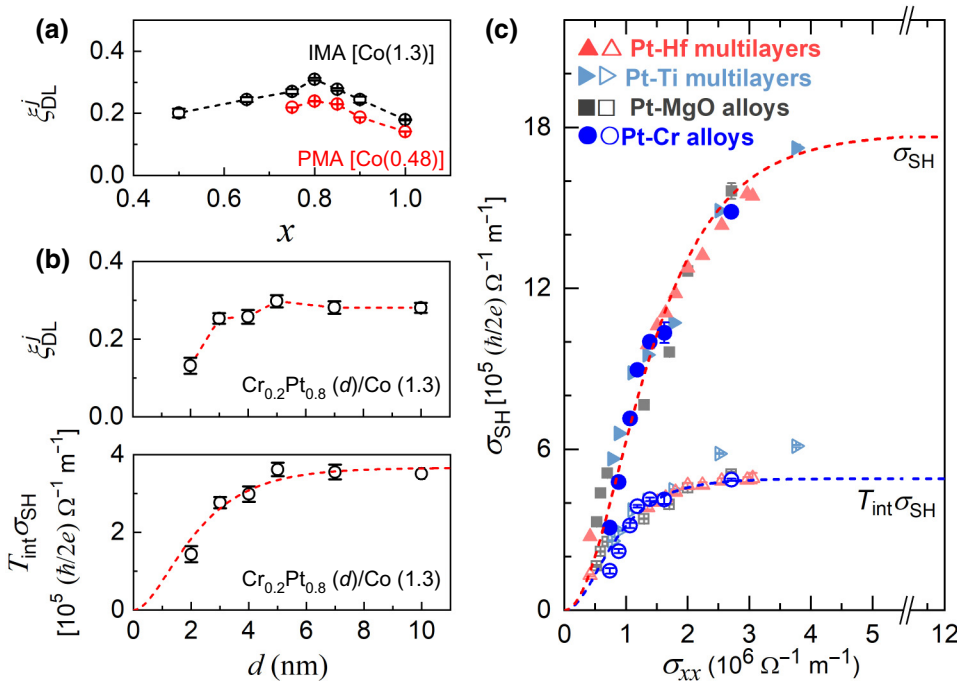


FIG. 4. (a) ξ_{DL}^j for $Cr_{1-x}Pt_x(5)/Co(1.3)$ (IMA) and $Cr_{1-x}Pt_x(5)/Co(0.48)$ (PMA) with different Pt concentration. (b) ξ_{DL}^j and $T_{int}\sigma_{SH}$ for $Cr_{0.2}Pt_{0.8}(d)/Co(1.3)$ with different thickness d . (c) Spin Hall conductivities $T_{int}\sigma_{SH}$ and σ_{SH} for $Cr_{1-x}Pt_x(5)/Co(1.3)$, $Pt_x(MgO)_x/Co$ [13], Pt-Hf multilayers/Co [22], and Pt-Ti multilayers/Co [23]. The lines are for guidance of eyes.

and overall coincide with those of other systems in which the intrinsic SHE is the dominant source of the spin current. This is striking evidence that the dominant mechanism of the spin-current generation in the $Cr_{1-x}Pt_x$ is the intrinsic SHE and that there is minimal additional spin-current generation via any other mechanisms (e.g., alternative spin Hall effect or orbital Hall effect from Cr or interfacial SOC effect) in this material. This is consistent with previous experimental [11–13] and theoretical [47] reports of the absence of any useful extrinsic spin Hall effect in Pt-rich alloys. We find that the characteristic variations of $T_{int}\sigma_{SH}$ and σ_{SH} with the longitudinal conductance for the Pt alloys and multilayers can be empirically fit by

$$T_{int}\sigma_{SH} = T_{int}\sigma_{SH0}(1 - \text{sech}(\sigma_{xx}/\sigma_{xx0})), \quad (4)$$

with the clean-limit apparent spin Hall conductivity $T_{int}\sigma_{SH0}$ of approximately equal to $4.95 \times 10^5 (\hbar/2e)\Omega^{-1} m^{-2}$ and with the characteristic conductivity σ_{xx0} of approximately equal to $5.0 \times 10^5 \Omega^{-1} m^{-1}$. We also find that the fieldlike SOTs of these samples are much smaller than the dampinglike torque (Fig. 8 in the Appendix), which is consistent with the intrinsic SHE in $Cr_{1-x}Pt_x$ alloys being the dominant source of the spin current associated with the SOTs.

In principle, interface-generated spin currents, if significant, can add to or subtract from the spin Hall spin current of HM/FM samples and affect the measured strength of SOTs. However, this usually seems to be a minor effect at magnetic interfaces. A recent SOT experiment [48] has established clean evidence that, under the same

electric field, the efficiency of spin-current generation by interfacial SOC effect [e.g., Rashba-Edelstein(-like) effect, inverse spin galvanic effect, or spin-filtering effect] should be at least 2–3 orders of magnitude smaller than that of Pt even when the interfacial SOC is quite strong (e.g., at $Ti/Fe_{0.6}Co_{0.2}B_{0.2}$ interfaces). The absence of a significant interfacial spin-current generation is also well supported by (i) a spin Seebeck and ISHE experiment that spin-current generation is absent at $Bi/Ag/Y_3Fe_5O_{12}$ and $Bi/Y_3Fe_5O_{12}$ interfaces [49,50] prepared by different techniques; (ii) the universal observation of strong scaling of the SOT efficiencies or the effective spin Hall ratio with the resistivity and the layer thickness of HMs [13,14,22,23,45,46,51,52] [see Figs. 3(b) and 3(c) for the $Cr_{1-x}Pt_x/Co$ case], topological insulators [53], nonmagnetic complex oxides [54]; (iii) the clear dependence of inverse spin Hall voltage on the spin-mixing conductance of the interfaces of magnetic oxides (e.g., $Y_3Fe_5O_{12}$) in spin Seebeck [49,50,55] and spin pumping [56]; and (iv) absence of SOT enhancement with increasing interfacial SOC strength [17,48,57] [see Figs. 4(a) and 11 in the Appendix for the $Cr_{1-x}Pt_x/Co$]. This is consistent with the theories [16,58–60] that interfacial SOC has negligible contribution to the dampinglike SOT via the two-dimensional Rashba-Edelstein(-like) effect of magnetic interfaces.

Here, we note that a previous loop shift study by Quan *et al.* [26] reported only a maximum ξ_{DL}^j of 0.1 for $Cr_{1-x}Pt_x(8)/Pt(0.4)/Co(0.9)$, however, those samples were annealed at 370 °C and thus likely have very strong spin memory loss at the Pt/Co interface [17]. Meanwhile, at

the optimal of that work, the resistivity $\text{Cr}_{1-x}\text{Pt}_x$ composition was only $56 \mu\Omega\text{cm}$ and the Co magnetization was as low as $820 \text{ emu}/\text{cm}^3$. ξ_{DL}^j of a HM/FM is positively correlated to the resistivity of the HM in this range, and a low magnetization may increase the spin-dephasing length to above the layer thickness of the FM and lower ξ_{DL}^j due to the resultant polarization rotation [41,42] of the reflected spin current at the top interface. We also notice that another loop-shift experiment [25] claimed ξ_{DL}^j of $0.2\text{--}0.34$ for Pt/Co and $0.9\text{--}0.94$ for $\text{Cr}_{1-x}\text{Pt}_x/\text{Co}$ in the composition range of $0.5 \leq x \leq 0.7$, which are surprisingly large compared to our expectation from the existing studies on Pt [9–14,19,22–24]. However, for reasons unknown, that work estimated resistivities that are a factor of 2–3 greater than ours in their calculation of ξ_{DL}^j and their $\text{Cr}_{1-x}\text{Pt}_x/\text{Co}$ samples also remained PMA in the wide concentration range of $x = 0.5\text{--}1$ even when t_{Co} was as large as 1.6 nm. The latter is in contrast to our observation that the $\text{Cr}_{1-x}\text{Pt}_x/\text{Co}$ becomes in-plane magnetized when $x \leq 0.65$.

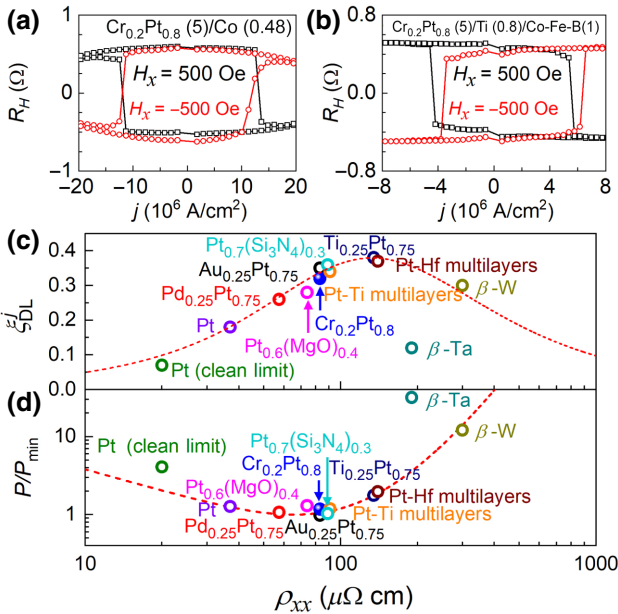


FIG. 5. Hall resistance vs in-plane current density in the $\text{Cr}_{0.2}\text{Pt}_{0.8}$ layer for (a) the $\text{Cr}_{0.2}\text{Pt}_{0.8}(5)/\text{Co}(0.48)$ and (b) the $\text{Cr}_{0.2}\text{Pt}_{0.8}(5)/\text{Ti}(0.8)/\text{Fe}_{0.6}\text{Co}_{0.2}\text{B}_{0.2}(1)$ under in-plane field of $\pm 500 \text{ Oe}$. (c) ξ_{DL}^j and ρ_{xx} for spin Hall metal/FM bilayers. The spin Hall metals are Pt, $\text{Cr}_{0.2}\text{Pt}_{0.8}$, $\text{Ti}_{0.25}\text{Pt}_{0.75}$ [21], $\text{Pt}_{0.6}(\text{MgO})_{0.4}$ [13], $\text{Au}_{0.25}\text{Pt}_{0.75}$ [11], $\text{Ti}_{0.25}\text{Pt}_{0.75}$ [11], $\text{Pt}_{0.7}(\text{Si}_3\text{N}_4)_{0.3}$ [27], $\text{Pd}_{0.25}\text{Pt}_{0.75}$ [12], $\beta\text{-Ta}$ [1], $\beta\text{-W}$ [3], and clean-limit Pt [62]. The dashed line in (c) represents the plot of Eq. (5), which indicates maximization of ξ_{DL}^j for Pt-based HM/FM systems in the resistivity range of $80\text{--}160 \mu\Omega \text{ cm}$. (d) Normalized power consumption of SOT MTJs based on different spin Hall metals as estimated using Eq. (6). The dashed line in (d) plots the power consumption expected for a spin Hall metal with ξ_{DL}^j and ρ_{xx} following Eq. (5). P_{\min} is the minimum value of power predicted by the dashed line.

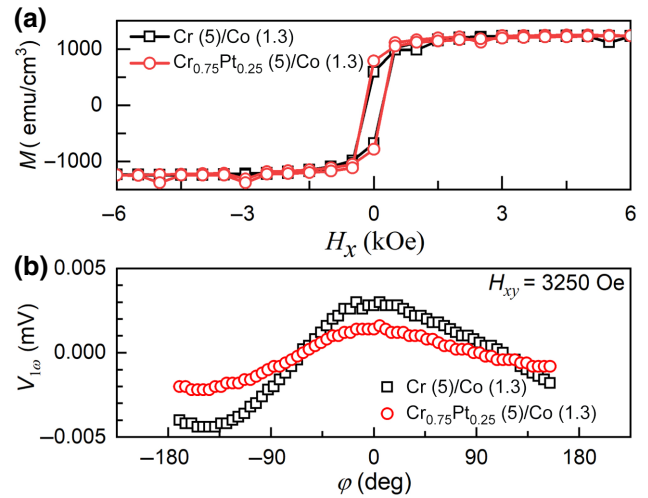


FIG. 6. (a) In-plane magnetization vs in-plane magnetic field and (b) first-harmonic Hall voltage response $V_{1\omega}$ vs in-plane angle of field (φ) with respect to the current (field = 3250 Oe) for $\text{Cr}(5 \text{ nm})/\text{Co}(1.3 \text{ nm})$ and $\text{Cr}_{0.75}\text{Pt}_{0.25}(5 \text{ nm})/\text{Co}(1.3 \text{ nm})$. The very small magnitude and the absence of a $\sin 2\varphi$ dependence of $V_{1\omega}$ indicates a strong anisotropy in the film plane that prevents magnetization rotation by the in-plane magnetic field in harmonic Hall voltage response analysis.

regardless of t_{Co} or when t_{Co} is $\geq 1.3 \text{ nm}$ regardless of the Pt concentration. Note that the $\text{Cr}_{1-x}\text{Pt}_x(8)/\text{Pt}(0.4)/\text{Co}(0.9)$ bilayers in Ref. [25] also required postgrowth annealing at 370°C to obtain PMA for the thin Co in the composition range of $(0.5 \leq x \leq 1)$. Finally, we do not attribute the large discrepancies of the ξ_{DL}^j values in this work and Refs. [25,26] to the measurement techniques since loop shift and HHVR techniques can yield consistent SOT results in other material systems (see detailed discussions in Ref. [61]).

D. Practical impact

Finally, we note that $\text{Cr}_{0.2}\text{Pt}_{0.8}$, which has $\rho_{xx} \approx 80 \mu\Omega \text{ cm}$, $\lambda_s \approx 1.6 \text{ nm}$, $\theta_{\text{SH}} \approx 0.7$, is a compelling spin Hall metal for technological applications. As shown in Fig. 5(a), a 5-nm $\text{Cr}_{0.2}\text{Pt}_{0.8}$ can switch a Co layer with high

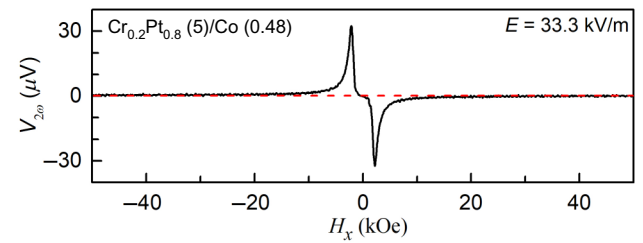


FIG. 7. Second-harmonic Hall voltage response ($V_{2\omega}$) vs in-plane magnetic field (H_x) for the $\text{Cr}_{0.2}\text{Pt}_{0.8}(5 \text{ nm})/\text{Co}(0.48 \text{ nm})$, suggesting negligible anomalous Nernst effect.

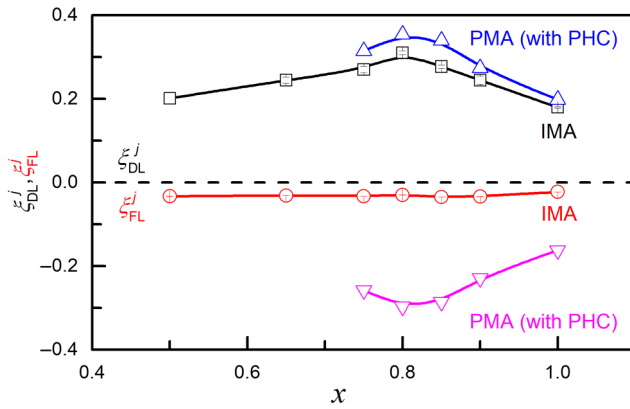


FIG. 8. Dependence on the Pt concentration of the spin-torque efficiencies (ξ_{DL}^j and ξ_{FL}^j) for the $\text{Cr}_{1-x}\text{Pt}_x(5 \text{ nm})/\text{Co}(0.48 \text{ nm})$ as determined from out-of-plane harmonic Hall voltage response (HHVR) measurement with the “planar Hall correction (PHC)” and for $\text{Cr}_{1-x}\text{Pt}_x(5 \text{ nm})/\text{Co}(1.3 \text{ nm})$ as determined from in-plane angle-dependent HHVR measurement. The values of ξ_{DL}^j and ξ_{FL}^j estimated with the PHC deviate significantly from the in-plane HHVR results.

PMA and coercivity ($H_k \approx 4900$ Oe, $H_c \approx 120$ Oe) at a current density of 1.2×10^7 A/cm². More impressively, as we show in Fig. 5(b), magnetization switching of strong PMA $\text{Cr}_{0.2}\text{Pt}_{0.8}(5)/\text{Ti}(0.8)/\text{Fe}_{0.6}\text{Co}_{0.2}\text{B}_{0.2}(1)$ ($H_k \approx 2500$ Oe, $H_c \approx 100$ Oe) can be achieved at a current

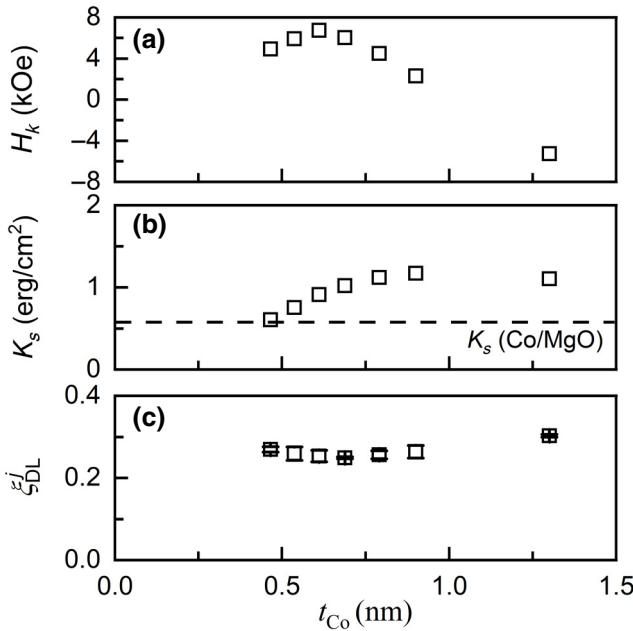


FIG. 9. Dependence on the Co thickness of (a) the perpendicular anisotropy field (H_k), (b) the interfacial magnetic anisotropy energy density (K_s), and (c) the dampinglike torque efficiency (ξ_{DL}^j) for the $\text{Cr}_{0.2}\text{Pt}_{0.8}/\text{Co}$ t_{Co} . K_s is negligible for the $\text{Cr}_{0.2}\text{Pt}_{0.8}(5 \text{ nm})/\text{Co}(0.48 \text{ nm})$ but strong for the $\text{Cr}_{0.2}\text{Pt}_{0.8}(5 \text{ nm})/\text{Co}(1.3 \text{ nm})$.

density as low as approximately equal to 4.8×10^6 A/cm² in the $\text{Cr}_{0.2}\text{Pt}_{0.8}$ layer. As compared in Fig. 5(c), $\text{Cr}_{0.2}\text{Pt}_{0.8}$ has high ξ_{DL}^j and relatively low ρ_{xx} that are similar to $\text{Pt}_{0.6}(\text{MgO})_{0.4}$ [13], $\text{Pt}_{0.7}(\text{Si}_3\text{N}_4)_{0.3}$ [27], $\text{Au}_{0.25}\text{Pt}_{0.75}$ [11], Pt-Ti multilayers [23]. Interestingly, the values of ξ_{DL}^j and $1/\sigma_{xx} = \rho_{xx}$ for various Pt alloys and multilayers approximately follow

$$\xi_{DL}^j = (2e/\hbar)T_{int}\sigma_{SH0}(1 - \text{sech}(1/\sigma_{xx0}))/\sigma_{xx}, \quad (5)$$

and statistically indicate maximization in the resistivity ($1/\sigma_{xx}$) range of 80 – 160 $\mu\Omega$ cm. Since ξ_{DL}^j expected from this scaling varies with ρ_{xx} only slightly in this resistivity range, the exact value of the largest ξ_{DL}^j and the corresponding resistivity of different specific material systems may vary due to varying strengths of spin backflow and spin memory loss at the interface and varying thicknesses and spin relaxation rates of the heavy metal and the ferromagnet in different studies. This should explain why the largest ξ_{DL}^j for the $\text{Cr}_{1-x}\text{Pt}_x(5)/\text{Co}(1.3)$ (IMA) and the $\text{Cr}_{1-x}\text{Pt}_x(5)/\text{Co}(0.48)$ (PMA) with different Pt concentration shows up at the composition $x = 0.2$ [$\rho_{xx} \approx 80$ $\mu\Omega$ cm, Fig. 4(a)] rather than lower x values [more resistive, Fig. 1(f)]. Since the switching power of a nanomagnet sit on a spin Hall metal channel (such as SOT MTJs) can be estimated as

$$P \propto [(1 + t_{FM}\sigma_{FM}/d\sigma_{xx})/\xi_{DL}^j]^2 \rho_{xx}, \quad (6)$$

we plot in Fig. 5(c) the normalized power consumption P of a $\text{Fe}_{0.6}\text{Co}_{0.2}\text{B}_{0.2}$ nanomagnet ($t_{FM} = 1.6$ nm, $1/\sigma_{FM} = 135$ $\mu\Omega$ cm) sit on different strong spin Hall metal channels as calculated using the measured values of $1/\sigma_{xx}$ and ξ_{DL}^j . The power consumption for the $\text{Cr}_{0.2}\text{Pt}_{0.8}$ device is comparable with the optimized $\text{Pt}_{0.6}(\text{MgO})_{0.4}$ [13], $\text{Pt}_{0.7}(\text{Si}_3\text{N}_4)_{0.3}$ [27], $\text{Au}_{0.25}\text{Pt}_{0.75}$ [11], $\text{Pd}_{0.25}\text{Pt}_{0.75}$ [12], and Pt-Ti multilayers [23], and represents the lower limit of the Pt-based alloys and multilayers as indicated by the red dashed line that plots the power consumption

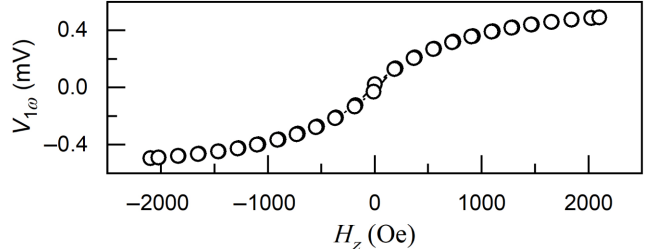


FIG. 10. First-harmonic Hall voltage response ($V_{1\omega}$) vs out-of-plane magnetic field (H_z) for the $\text{Cr}_{0.35}\text{Pt}_{0.65}(5 \text{ nm})/\text{Co}(0.48 \text{ nm})$, suggesting a perpendicular magnetic anisotropy that is too weak to allow for reliable out-of-plane harmonic Hall voltage response analysis.

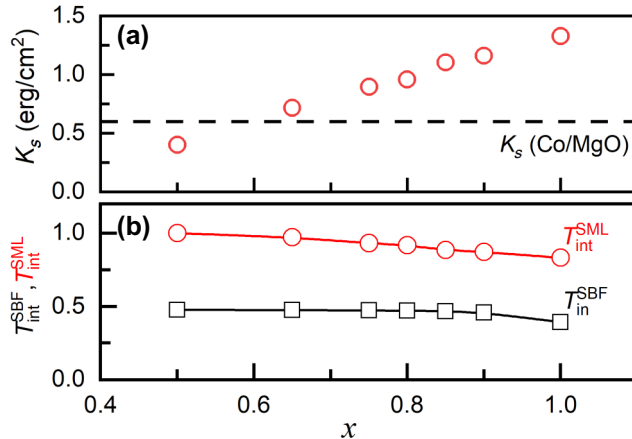


FIG. 11. Dependence on the Pt concentration x of (a) interfacial perpendicular magnetic anisotropy energy density (K_s) and (b) spin transparencies set by spin backflow [$T_{\text{int}}^{\text{Sbf}}$, as calculated following Eq. (3)] and by spin memory loss ($T_{\text{int}}^{\text{SML}}$, as calculated following the relation $T_{\text{int}}^{\text{SML}} \approx 1 - 0.23 K_s^{\text{ISOC}}$) for the $\text{Cr}_{1-x}\text{Pt}_x(5)/\text{Co}(1.3)/\text{MgO}$ samples. K_s for the $\text{Cr}_{0.5}\text{Pt}_{0.5}/\text{Co}(1.3)/\text{MgO}$ interface (approximately equal to 0.6 erg/cm^2) is smaller than that of the Co/MgO interface (approximately equal to 0.6 erg/cm^2) likely due to a non-negligible in-plane volume anisotropy of Co.

by using ξ_{DL}^j and σ_{xx} predicted by Eq. (5). Therefore, $\text{Cr}_{0.2}\text{Pt}_{0.8}$ is an excellent spin Hall metal that is comparable to the optimized Pt alloys and advantageous over β -Ta [1], β -W [3], clean-limit Pt [62], in terms of energy efficiency, impedance, and endurance when used in spin-orbit technologies.

III. CONCLUSIONS

In conclusion, we present that the dampinglike spin-orbit-torque efficiency of $\text{Cr}_{1-x}\text{Pt}_x/\text{Co}$ bilayers can be enhanced by tuning the Cr concentration in the $\text{Cr}_{1-x}\text{Pt}_x$ layer, with a maximal value of 0.31 at the optimal composition of $\text{Cr}_{0.2}\text{Pt}_{0.8}$. The efficiency of the spin-current generation in the $\text{Cr}_{1-x}\text{Pt}_x$ alloy is found to be dominated by the characteristic trade-off between the intrinsic spin Hall conductivity of Pt and the spin carrier lifetime in the dirty limit and coincide well with those of other Pt-based spin Hall metal systems. Cr turns out to be simply as effective as other metals, oxides, and nitrides (e.g., Hf, Au, Pd, Cu, Ti, MgO, and Si_3N_4) in enhancing the dampinglike spin-orbit torque generated by the spin Hall effect of a Pt host. We find no obvious evidence for spin-current generation by a mechanism other than the intrinsic SHE of Pt in $\text{Cr}_{1-x}\text{Pt}_x$. This work establishes the low-resistivity $\text{Cr}_{0.2}\text{Pt}_{0.8}$ as an energy-efficient SOT provider for magnetic memory and computing applications.

ACKNOWLEDGMENTS

This work is supported partly by the Strategic Priority Research Program of the Chinese Academy of Sciences

(XDB44000000) and by the National Natural Science Foundation of China (Grants No. 12274405 and No. 51901121).

APPENDIX

(Figures 6–11)

- [1] L. Liu, C.-F. Pai, Y. Li, H. W. Tseng, D. C. Ralph, and R. A. Buhrman, Spin-torque switching with the giant spin Hall effect of tantalum, *Science* **336**, 555 (2012).
- [2] I. M. Miron, K. Garello, G. Gaudin, P.-J. Zermatten, M. V. Costache, S. Auffret, S. Bandiera, B. Rodmacq, A. Schuhl, and P. Gambardella, Perpendicular switching of a single ferromagnetic layer induced by in-plane current injection, *Nature (London)* **476**, 189 (2011).
- [3] C.-F. Pai, L. Liu, Y. Li, H. W. Tseng, D. C. Ralph, and R. A. Buhrman, Spin transfer torque devices utilizing the giant spin Hall effect of tungsten, *Appl. Phys. Lett.* **101**, 122404 (2012).
- [4] G. Yu, P. Upadhyaya, Y. Fan, J. G. Alzate, W. Jiang, K. L. Wong, S. Takei, S. A. Bender, L.-T. Chang, Y. Jiang, *et al.*, Switching of perpendicular magnetization by spin-orbit torques in the absence of external magnetic fields, *Nat. Nanotechnol.* **9**, 548 (2014).
- [5] W. Jiang, P. Upadhyaya, W. Zhang, G. Yu, M. B. Jungfleisch, F. Y. Fradin, J. E. Pearson, Y. Tserkovnyak, K. L. Wang, O. Heinonen, *et al.*, Blowing magnetic skyrmion bubbles, *Science* **349**, 283 (2015).
- [6] H. Qiu, L. Zhou, C. Zhang, J. Wu, Y. Tian, S. Cheng, S. Mi, H. Zhao, Q. Zhang, D. Wu, *et al.*, Ultrafast spin current generated from an antiferromagnet, *Nat. Phys.* **17**, 388 (2021).
- [7] L. Zhu, L. Zhu, S. Shi, D. C. Ralph, and R. A. Buhrman, Energy-efficient ultrafast SOT-MRAMs based on low-resistivity spin Hall metal $\text{Au}_{0.25}\text{Pt}_{0.75}$, *Adv. Electron. Mater.* **6**, 1901131 (2020).
- [8] T. H. Dang, *et al.*, Ultrafast spin-currents and charge conversion at 3D–5D interfaces probed by time-domain terahertz spectroscopy, *Appl. Phys. Rev.* **7**, 041409 (2020).
- [9] G. D. H. Wong, W. C. Law, F. N. Tan, W. L. Gan, C. C. I. Ang, Z. Xu, C. S. Seet, and W. S. Lew, Thermal behavior of spin-current generation in $\text{Pt}_x\text{Cu}_{1-x}$ devices characterized through spin-torque ferromagnetic resonance, *Sci. Rep.* **10**, 9631 (2020).
- [10] M.-H. Nguyen, M. Zhao, D. C. Ralph, and R. A. Buhrman, Enhanced spin Hall torque efficiency in $\text{Pt}_{100-x}\text{Al}_x$ and $\text{Pt}_{100-x}\text{Hf}_x$ alloys arising from the intrinsic spin Hall effect, *Appl. Phys. Lett.* **108**, 242407 (2016).
- [11] L. Zhu, D. C. Ralph, and R. A. Buhrman, Highly Efficient Spin-Current Generation by the Spin Hall Effect in $\text{Au}_{1-x}\text{Pt}_x$, *Phys. Rev. Appl.* **10**, 031001 (2018).
- [12] L. Zhu, K. Sobotkiewich, X. Ma, X. Q. Li, D. C. Ralph, and R. A. Buhrman, Strong damping-like spin-orbit torque and tunable Dzyaloshinskii–Moriya interaction generated by low-resistivity $\text{Pd}_{1-x}\text{Pt}_x$ alloys, *Adv. Funct. Mater.* **29**, 1805822 (2019).

- [13] L. Zhu, L. Zhu, M. L. Sui, D. C. Ralph, and R. A. Buhrman, Variation of the giant intrinsic spin Hall conductivity of Pt with carrier lifetime, *Sci. Adv.* **5**, eaav8025 (2019).
- [14] C. Y. Hu and C. F. Pai, Benchmarking of spin-orbit torque switching efficiency in Pt alloys, *Adv. Quantum Technol.* **3**, 2000024 (2020).
- [15] C. Pai, Y. Ou, L. H. Vilela-Leão, D. C. Ralph, and R. A. Buhrman, Dependence of the efficiency of spin Hall torque on the transparency of Pt/ferromagnetic layer interfaces, *Phys. Rev. B* **92**, 064426 (2015).
- [16] P. M. Haney, H. W. Lee, K. J. Lee, A. Manchon, and M. D. Stiles, Current induced torques and interfacial spin-orbit coupling: Semiclassical modeling, *Phys. Rev. B* **87**, 174411 (2013).
- [17] L. Zhu, D. C. Ralph, and R. A. Buhrman, Spin-Orbit Torques in Heavy-Metal-Ferromagnet Bilayers with Varying Strengths of Interfacial Spin-Orbit Coupling, *Phys. Rev. Lett.* **122**, 077201 (2019).
- [18] L. Zhu, D. C. Ralph, and R. A. Buhrman, Effective Spin-Mixing Conductance of Heavy-Metal-Ferromagnet Interfaces, *Phys. Rev. Lett.* **123**, 057203 (2019).
- [19] L. Zhu, L. Zhu, and R. A. Buhrman, Fully Spin-Transparent Magnetic Interfaces Enabled by the Insertion of a Thin Paramagnetic NiO Layer, *Phys. Rev. Lett.* **126**, 107204 (2021).
- [20] T. Tanaka, H. Kontani, M. Naito, T. Naito, D. S. Hirashima, K. Yamada, and J. Inoue, Intrinsic spin Hall effect and orbital Hall effect in 4d and 5d transition metals *Phys. Rev. B* **77**, 165117 (2008).
- [21] L. Zhu and D. C. Ralph, Strong variation of spin-orbit torque with relative spin relaxation rates in ferrimagnets, *arXiv:2210.11042*.
- [22] L. Zhu, L. Zhu, S. Shi, M. Sui, D. C. Ralph, and R. A. Buhrman, Enhancing Spin-Orbit Torque by Strong Interfacial Scattering from Ultrathin Insertion Layers, *Phys. Rev. Appl.* **11**, 061004 (2019).
- [23] L. Zhu and R. A. Buhrman, Maximizing Spin-Orbit-Torque Efficiency of Pt-Ti Multilayers: Trade-Off Between Intrinsic Spin Hall Conductivity and Carrier Lifetime, *Phys. Rev. Appl.* **12**, 051002 (2019).
- [24] L. Zhu, D. C. Ralph, and R. A. Buhrman, Maximizing spin-orbit torque generated by the spin Hall effect of Pt, *Appl. Phys. Rev.* **8**, 031308 (2021).
- [25] C. Hu, Y. Chiu, C. Tsai, C. Huang, K. Chen, C. Peng, C. Lee, M. Song, Y. Huang, S. Lin, and C. Pai, Toward 100% spin-orbit torque efficiency with high spin-orbital Hall conductivity Pt-Cr alloys, *ACS Appl. Electron. Mater.* **4**, 1099 (2022).
- [26] J. Quan, X. Zhao, W. Liu, L. Liu, Y. Song, Y. Li, X. Zhao, and Z. Zhang, Enhancement of spin-orbit torque and modulation of Dzyaloshinskii-Moriya interaction in $\text{Pt}_{100-x}\text{Cr}_x/\text{Co}/\text{AlO}_x$ trilayer, *Appl. Phys. Lett.* **117**, 222405 (2020).
- [27] X. Lin, J. Li, L. Zhu, X. Xie, Q. Liu, D. Wei, G. Yuan, and L. Zhu, Strong enhancement of spin-orbit torques in ferrimagnetic $\text{Pt}_x(\text{Si}_3\text{N}_4)_{1-x}/\text{CoTb}$ bilayers by Si_3N_4 doping, *Phys. Rev. B* **106**, L140407 (2022).
- [28] D. Qu, S. Y. Huang, and C. L. Chien, Inverse spin Hall effect in Cr: Independence of antiferromagnetic ordering, *Phys. Rev. B* **92**, 020418(R) (2015).
- [29] C. Du, H. Wang, F. Yang, and P. C. Hammel, Systematic variation of spin-orbit coupling with d -orbital filling: Large inverse spin Hall effect in 3d transition metals, *Phys. Rev. B* **90**, 140407(R) (2014).
- [30] A. Bose, H. Singh, V. K. Kushwaha, S. Bhuktare, S. Dutta, and A. A. Tulapurkar, Sign Reversal of Fieldlike Spin-Orbit Torque in an Ultrathin Cr/Ni Bilayer, *Phys. Rev. Appl.* **9**, 014022 (2018).
- [31] D. Jo, D. Go, and H.-W. Lee, Gigantic intrinsic orbital Hall effects in weakly spin-orbit coupled metals, *Phys. Rev. B* **98**, 214405 (2018).
- [32] S. Lee, M.-G. Kang, D. Go, D. Kim, J.-H. Kang, T. Lee, G.-H. Lee, J. Kang, N. J. Lee, Y. Mokrousov, *et al.*, Efficient conversion of orbital Hall current to spin current for spin-orbit torque switching, *Commun. Phys.* **4**, 234 (2021).
- [33] M. J. Besnus and A. J. P. Meyer, Order states and magnetic states of CrPt_3 , *Phys. Status Solidi B* **55**, 521 (1973).
- [34] M. J. Besnus and A. J. P. Meyer, Magnetic properties of the ordered and disordered CrPt_3 and CrPt phases, *Phys. Status Solidi B* **58**, 533 (1973).
- [35] C. O. Avci, K. Garello, M. Gabureac, A. Ghosh, A. Fuhrer, S. F. Alvarado, and P. Gambardella, Interplay of spin-orbit torque and thermoelectric effects in ferromagnet/normal-metal bilayers, *Phys. Rev. B* **90**, 224427 (2014).
- [36] M. Hayashi, J. Kim, M. Yamanouchi, and H. Ohno, Quantitative characterization of the spin-orbit torque using harmonic Hall voltage measurements, *Phys. Rev. B* **89**, 144425 (2014).
- [37] A. Ghosh, K. Garello, C. O. Avci, M. Gabureac, and P. Gambardella, Interface-Enhanced Spin-Orbit Torques and Current-Induced Magnetization Switching of $\text{Pt}/\text{Co}/\text{AlO}_x$ Layers, *Phys. Rev. Appl.* **7**, 014004 (2017).
- [38] Q. Liu, L. Zhu, X. S. Zhang, D. Muller, and D. C. Ralph, Giant bulk spin-orbit torque and efficient electrical switching in single ferrimagnetic FeTb layers with strong perpendicular magnetic anisotropy, *Appl. Phys. Rev.* **9**, 021402 (2022).
- [39] J. Torrejon, J. Kim, J. Sinha, S. Mitani, M. Hayashi, M. Yamanouchi, and H. Ohno, Interface control of the magnetic chirality in CoFeB/MgO heterostructures with heavy-metal underlayers, *Nat. Commun.* **5**, 4655 (2014).
- [40] S. Karimeddin, T. M. Cham, D. C. Ralph, and Y. K. Luo, Sagnac interferometry for high-sensitivity optical measurements of spin-orbit torque, *arXiv: 2109.13759*.
- [41] Y. Ou, C.-F. Pai, S. Shi, D. C. Ralph, and R. A. Buhrman, Origin of fieldlike spin-orbit torques in heavy metal/ferromagnet/oxide thin film heterostructures, *Phys. Rev. B* **94**, 140414(R) (2016).
- [42] Z. Luo, Q. Zhang, Y. Xu, Y. Yang, X. Zhang, and Y. Wu, Spin-Orbit Torque in a Single Ferromagnetic Layer Induced by Surface Spin Rotation, *Phys. Rev. Appl.* **11**, 064021 (2019).
- [43] Y.-T. Chen, S. Takahashi, H. Nakayama, M. Althammer, S. T. B. Goennenwein, E. Saitoh, and G. E. W. Bauer, Theory of spin Hall magnetoresistance, *Phys. Rev. B* **87**, 144401 (2013).
- [44] V. P. Amin and M. D. Stiles, Spin transport at interfaces with spin-orbit coupling: Phenomenology, *Phys. Rev. B* **94**, 104420 (2016).
- [45] M.-H. Nguyen, D. C. Ralph, and R. A. Buhrman, Spin Torque Study of the Spin Hall Conductivity and Spin

- Diffusion Length in Platinum Thin Films with Varying Resistivity, *Phys. Rev. Lett.* **116**, 126601 (2016).
- [46] E. Sagasta, Y. Omori, M. Isasa, M. Gradhand, L. E. Hueso, Y. Niimi, Y. Otani, and F. Casanova, Tuning the spin Hall effect of Pt from the moderately dirty to the superclean regime, *Phys. Rev. B* **94**, 060412(R) (2016).
- [47] S. Lowitzer, M. Gradhand, D. Ködderitzsch, D. V. Fedorov, I. Mertig, and H. Ebert, Extrinsic and Intrinsic Contributions to the Spin Hall Effect of Alloys, *Phys. Rev. Lett.* **106**, 056601 (2011).
- [48] L. Zhu and R. A. Buhrman, Absence of Significant Spin-Current Generation in Ti/Fe–Co–B Bilayers with Strong Interfacial Spin-Orbit Coupling, *Phys. Rev. Appl.* **15**, L031001 (2021).
- [49] D. Yue, W. Lin, J. Li, X. Jin, and C. L. Chien, Spin-to-Charge Conversion in Bi Films and Bi/Ag Bilayers, *Phys. Rev. Lett.* **121**, 037201 (2018).
- [50] D. Yue, W. Lin, and C. L. Chien, Negligible spin-charge conversion in Bi films and Bi/Ag(Cu) bilayers, *APL Mater.* **9**, 050904 (2021).
- [51] Q. Hao and G. Xiao, Giant Spin Hall Effect and Switching Induced by Spin-Transfer Torque in a W/Co₄₀Fe₄₀B₂₀/MgO Structure with Perpendicular Magnetic Anisotropy, *Phys. Rev. Appl.* **3**, 034009 (2015).
- [52] X. Shu, J. Zhou, J. Deng, W. Lin, J. Yu, L. Liu, C. Zhou, P. Yang, and J. Chen, Spin-orbit torque in chemically disordered and L1₁-ordered Cu_{100-x}Pt_x, *Phys. Rev. Mater.* **3**, 114410 (2019).
- [53] Z. Chi, Y.-C. Lau, X. Xu, T. Ohkubo, K. Hono, and M. Hayashi, The spin Hall effect of Bi-Sb alloys driven by thermally excited Dirac-like electrons, *Sci. Adv.* **6**, eaay2324 (2020).
- [54] T. Nan, T. J. Anderson, J. Gibbons, K. Hwang, N. Campbell, H. Zhou, Y. Q. Dong, G. Y. Kim, D. F. Shao, T. R. Paudel, *et al.*, Anisotropic spin-orbit torque generation in epitaxial SrIrO₃ by symmetry design, *PNAS* **116**, 16186 (2019).
- [55] O. Mosendz, J. E. Pearson, F. Y. Fradin, G. E. W. Bauer, S. D. Bader, and A. Hoffmann, Quantifying Spin Hall Angles from Spin Pumping: Experiments and Theory, *Phys. Rev. Lett.* **104**, 046601 (2010).
- [56] Z. Qiu, J. Li, D. Hou, E. Arenholz, A. T. N'Diaye, A. Tan, K. Uchida, K. Sato, S. Okamoto, Y. Tserkovnyak, *et al.*, Spin-current probe for phase transition in an insulator, *Nat. Commun.* **7**, 12670 (2016).
- [57] L. Zhu, L. Zhu, D. C. Ralph, and R. A. Buhrman, Origin of Strong Two-Magnon Scattering in Heavy-Metal/Ferromagnet/Oxide Heterostructures, *Phys. Rev. Appl.* **13**, 034038 (2020).
- [58] X. Wang and A. Manchon, Diffusive Spin Dynamics in Ferromagnetic Thin Films with a Rashba Interaction, *Phys. Rev. Lett.* **108**, 117201 (2012).
- [59] A. Manchon and S. Zhang, Theory of spin torque due to spin-orbit coupling, *Phys. Rev. B* **79**, 094422 (2009).
- [60] P. M. Haney, H. W. Lee, K. J. Lee, A. Manchon, and M. D. Stiles, Current-induced torques and interfacial spin-orbit coupling, *Phys. Rev. B* **88**, 214417 (2013).
- [61] L. Zhu, D. C. Ralph, and R. A. Buhrman, Lack of Simple Correlation between Switching Current Density and Spin-Orbit-Torque Efficiency of Perpendicularly Magnetized Spin-Current-Generator–Ferromagnet Heterostructures, *Phys. Rev. Appl.* **15**, 024059 (2021).
- [62] L. Liu, T. Moriyama, D. C. Ralph, and R. A. Buhrman, Spin-Torque Ferromagnetic Resonance Induced by the Spin Hall Effect, *Phys. Rev. Lett.* **106**, 036601 (2011).